High Sensitivity and High Throughput Magnetic Flow CMOS Cytometers with 2D Oscillator Array and Inter-Sensor Spectrogram Cross-correlation

Hao Tang, Member, IEEE, Suresh Venkatesh, Member, IEEE, Zhongtian Lin, Member, IEEE, Xuyang Lu, Member, IEEE, Hooman Saeeidi, Mehdi Javanmard, Member, IEEE, and Kaushik Sengupta, Senior Member, IEEE

Abstract—In the paper, we present an integrated flow cytometer with a 2D array of magnetic sensors based on dual-frequency oscillators in a 65-nm CMOS process, with the chip packaged with microfluidic controls. The sensor architecture and the presented array signal processing allows uninhibited flow of the sample for high throughput without the need for hydrodynamic focusing to a single sensor. To overcome the challenge of sensitivity and specificity that comes as a trade off with high throughout, we perform two levels of signal processing. First, utilizing the fact that a magnetically tagged cell is expected to excite sequentially an array of sensors in a time-delayed fashion, we perform inter-site cross-correlation of the sensor spectrograms that allows us to suppress the probability of false detection drastically, allowing theoretical sensitivity reaching towards sub-ppM levels that is needed for rare cell or circulating tumor cell detection. In addition, we implement two distinct methods to suppress correlated low frequency drifts of singular sensors—one with an on-chip sensor reference and one that utilizes the frequency dependence of the susceptibility of super-paramagnetic magnetic beads that we deploy as tags. We demonstrate these techniques on a 7×7 sensor array in 65 nm CMOS technology packaged with microfluidics with magnetically tagged dielectric particles and cultu lymphoma cancer cells.

Index Terms—Biosensor, magnetic flow cytometer, flow cytometry, LC-tank oscillator, frequency tracking, microfluidics, superparamagnetic, point-of-care diagnostics.

I. Introduction

Flow cytometers (FC) allow detection and measurement of biophysical and biochemical properties of a population of cells. It is an essential technology for cell counting, cell sorting, determining cell characteristics and function, detection of microorganisms, bio-markers and diagnosis of health disorders such as blood cancers. Considering the importance of FCs, there has been research efforts for large-scale integration and enabling multi-functionalities focusing on both label-free and labeled methods for detection. Label-free method focusing on distinguishing features in the physical properties of cells, such as size, mass or electrical impedance has been demonstrated with laser scattering [1], electrochemical impedance spectroscopy(EIS) [2]–[6], buoyant mass spectroscopy [7], and for sorting using acoustic waves [8], and inertial flow [9]. However, cells can be highly heterogeneous which makes it extremely challenging to distinguish among multiple classes of cells with single a physical parameter [10]. On the other hand, fluorescent or magnetic labels added to the cell samples, based on highly specific antigen-antibody interactions, allows remarkable specificity that is critical for isolation and identification of rare cells [11]–[18]. The use of fluorescent molecules in the traditional FC requires elaborate sample preparation such as lysing of red blood cells (RBCs) to prevent autofluorescence from RBCS, and interfering with the measurement [19]. On the other hand, the non-magnetic nature of biological cells allow detection of magnetically labeled cells in whole blood samples without the need for RBCs lysis [20].

The core component of the MFC is the magnetic sensor that converts the external magnetic field variation into a measurable electrical signal, such as resistance, voltage or impedance [21]. A majority of the prior works on high sensitivity magnetic sensing have based on utilizing giant magneto-resistance (GMR) [22]–[26] or magneto-impedance GMI [27], [28], and Hall effect [29], [30]. This is summarized in Fig. 1. As magnetic particles (MPs) pass over the GMR spin-valve sensor, their fringe fields flip the magnetization direction of the free layer, thereby changing the DC resistance of the sensor. For GMI sensors, the fringe fields modify the magnetic permeability of the GMI sensor, thereby changing the skin depth of AC current inside the GMI, which can be readout as AC impedance. On the other hand, when MPs pass over a μHall sensor, the extra vertical magnetic field induced by the MPs will deflect extra charged carriers to the measurement terminals, thereby changing the output DC voltage (Fig. 1). All of these methods measure the strength of the extra magnetic field generated by the MPs, which is determined by the degree of magnetization of MPs. In order

H. Tang was with the Department of Electrical and Computer Engineering, Princeton University, Princeton, NJ, 08544, USA. e-mail: haot@princeton.edu.

S. Venkatesh was the Department of Electrical and Computer Engineering, Princeton University, Princeton, NJ, 08544, USA. He is now with the Department of Electrical and Computer Engineering, North Carolina State University, Raleigh, NC 27695, USA.

Z. Lin was with the Department of Electrical and Computer Engineering, Rutgers University, Piscataway, NJ, 08854, USA.

X.Lu was with the Department of Electrical and Computer Engineering, Princeton University, Princeton, NJ, 08544, USA. He is now with the Department of Electrical and Computer Engineering, University of Michigan-Shanghai Jiao Tong University Joint Institute, Shanghai, China.

H.Saeeidi was with the Department of Electrical and Computer Engineering, Princeton University, Princeton, NJ, 08544, USA.

M.Javanmard is with the Department of Electrical and Computer Engineering, Rutgers University, Piscataway, NJ, 08854, USA.

K.Sengupta is with the Department of Electrical and Computer Engineering, Princeton University, Princeton, NJ, 08544, USA.

The work was partially funded by National Science Foundation grant number 1711165 and Princeton Catalysis Institute.

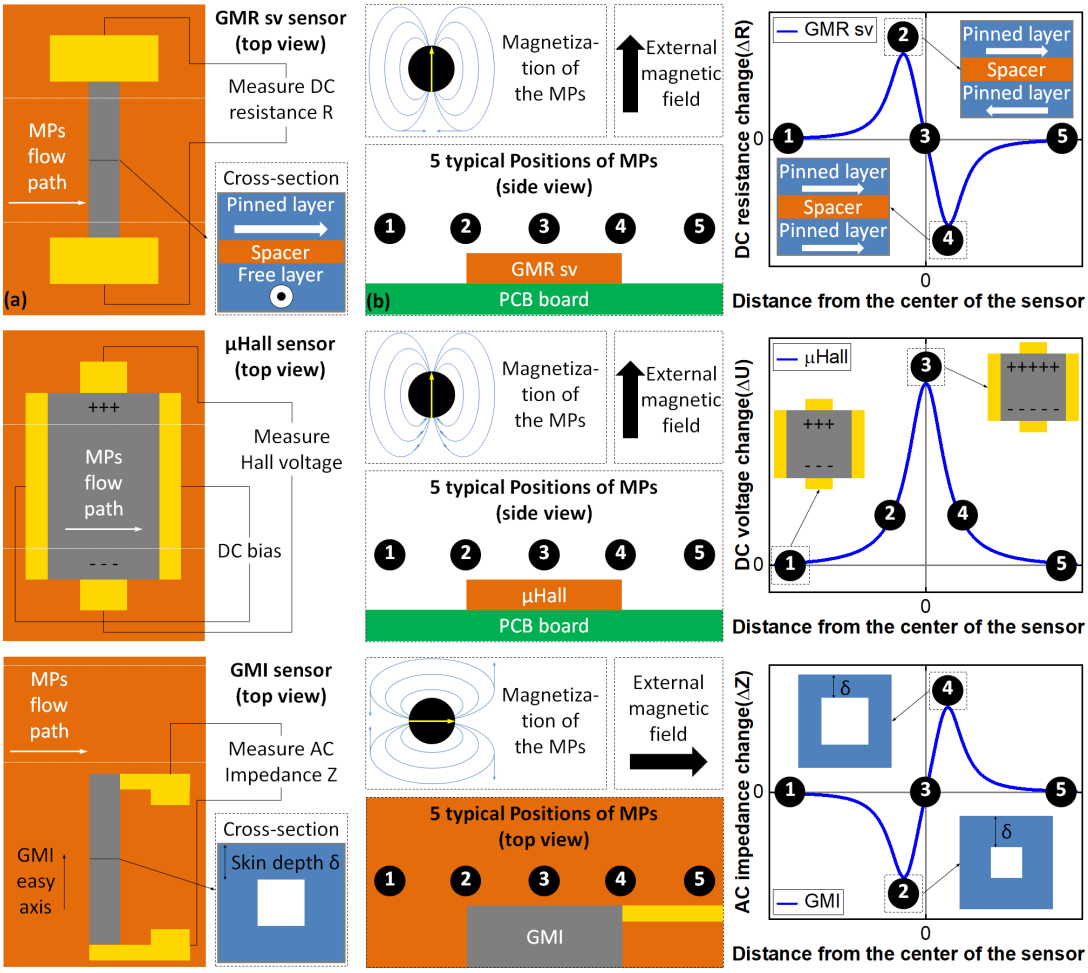

Fig. 1. Principle of operation of prior works in magnetic flow cytometers utilizing (a) Giant magneto resistance [22], (b) Hall effect [29], [30] and (c) giant magneto impedance [27], [28].

to extract measurable signal-to-noise ratio (SNR), the MPs are required to be in full spontaneous magnetization state. As an example, 2.8 µm Dynabeads requires an approximately 140 mT external magnetic field, typically generated by an external magnet [31]. In addition to the requirements of external magnets, integration of GMR and GMI sensors are non-compatible with current CMOS fabrication processes.

To allow compatibility with CMOS based platforms, prior works have also demonstrated magnetic sensing based on spiral coils [19], [32]–[35]. In [19], for example, the cytometer measures the changes in magnetic flux density in the spiral coil as the MPs pass over the sensor. This does require an external magnet to magnetize the MPs and the singular sensor (on which the sample is focused to flow on) limits the achievable throughput. In [36], oscillator-based reactance sensors were employed for label-free single-cell analysis using dielectric spectroscopy at microwave frequencies. The samples had to be hydro-focused to one channel to allow careful positioning of the cells, limiting the achievable throughput. In [32]–[34], magnetic sensing was achieved with integrated LC-oscillators that respond to the magnetization change in the presence of MPs. Employing drift cancellation with reference oscillators, bio-molecular sensing with hybridization assays on chip was demonstrated. In high throughput flow cytometry, however, the dynamic nature of the flows puts additional constraints on long term averaging, and requires co-design with microfluidics and specific signal processing techniques to reduce false positives and negatives below the rare cell concentrations.

In this paper, we present an approach for high throughput and high sensitivity assays with a 2D array of oscillator-based sensors integrated in a CMOS chip [37]. To allow the high throughput we do not focus the flow over a single sensor, but let the sample flow uninhibited through a microfluidic channel packaged on the surface of the chip allowing multi-site detection. In addition, to achieve high specificity and reduce false positives/negatives compared to a single sensor, we exploit cross-correlation of the spectrogram of the neighboring pixel sensors. A flowing magnetically-tagged cell is expected to excite the sensor arrays in a time-delayed fashion (depending on flow velocity), and this is reflected in a peak in the multi-dimensional cross-correlation space at the respective time delay. Single sensor false positives/negatives can therefore be eliminated through a thresholding of the cross-correlation output. The time delay in the cross-correlation output also effectively gives us a method to perform on-chip measurement of the flow rate without employing any external

velocity measurement sensor. In summary, moving from a single sensor to a sensor array can allow us a higher throughput eliminating the need for sample focusing, allow us trackign capabilities and higher sensitivity due to repeated time-delayed measurements over the spatial distribution of the sensors as the sample flows.We demonstrate the functionality of the array with magnetic bead flows and detection of lymphoma cancer cells with Maritriptase, and Anti-maritriptase monoclonal antibody with magnetic bead complex. The paper is organized as follows. Section II discusses the sensor architecture and the spectrogram cross-correlation approach for high specificity and high throughput. The sensor design is elaborated in Section III. Measurement results are presented in Section IV followed by Conclusions.

II. 2D Magnetic Sensor Array Architecture with Inter-site Spectrogram Cross-correlation

The performance metrics for a FC is highly application specific. However, a few guidelines can be formulated to guide the development of the sensor array.

- High specificity: Firstly, the sensor must allow low false detection rate. This is critically important to detect circulating tumor cells (CTCs) where 1-10 CTCs might be in circulation amidst 1-10 million white blood cells. Therefore, the false detection rate should be at least at sub-the ppm level.
- High throughput: CTCs need to be detected before cell lyses. Therefore, the flow rate should allow more than one million cells to be detected with high sensitivity and specificity within a few hours.
- Miniaturization and low cost: A scalable, integrated and low-cost diagnosis platform is key. Therefore, minimizing external components and full CMOS compatibility is preferred.

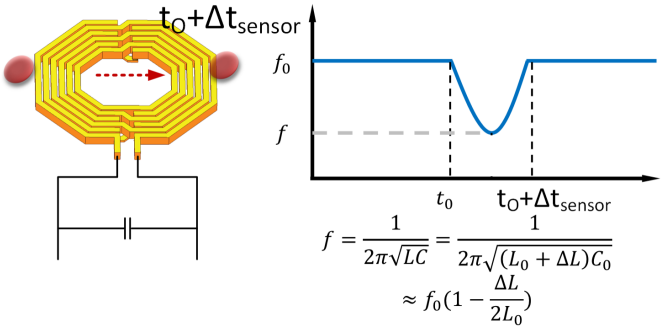

Fig. 2. Ideal dynamic response of oscillator spectrogram output due to the passage of magnetically-labeled cell.

The operation of a single sensor is easy to understand and illustrated in Fig. 4. When the magnetic particles labeled biosamples pass through the sensor core area, it introduces a dynamic change in the local magnetic field. The effective inductance of the LC-tank changes from L to L + ΔL, resulting in a change in oscillator frequency from f_0 to $f_0 - \Delta f \approx f_0(1 - \frac{\Delta L}{2L})$. This frequency change happens over a time period (Δt_{sensor})as the particle passes over the sensor area with a flow velocity. In reality, the sensor suffers from several non-idealities including high frequency noise and long term drifts that result in false detections. In addition, a single sensor limits the throughput needed to achieve in practical FCs.

The deployment of the array architecture and inter-site cross-correlation is precisely to address the limitations of sensitivity and throughput of a single sensor. The concept is illustrated in Fig. 3. The chip is interfaced with a microfluidic channel and the sample is flown over the surface of the chip. A thin PDMS surface separates the chip from the channel to allow the MPS be in the magnetic near-field of the sensors. As shown in the figure, the sensor array is arranged into a honeycomb lattice to prevent missing samples. Now, consider a single MP passing over an array of oscillator sensors sequentially (OSC01, OSC08, OSC14, OSC21, OSC28, OSC36, OSC43), and locally disturbing the magnetic fields. An example spectrogram of the sensor array is shown in the figure for illustrative purposes. The flowing MP creates a spike down in the spectrogram corresponding to oscillator (OSC01) at time T_1. After time Δt, as the MP passes over the next sensor (OSC08), it creates a similar downward spike in the corresponding sensor output as expected. This continues sequentially with other sensors as well with the final spike at T_6 in OSC36. However, there can be false spikes in sensors and missing detection. As an example, OSC01, OSC14 and OSC28 display false positives, while OSC14 completely misses the detection (false negative). In addition, each sensor might display a long term drift, which can be correlated across the chip, along with a reference sensor. Here, by false positive, we imply if a sensor responds positively even when no magnetically labeled cells have passed over it. Loose magnetic beads floating in the sample can also lead to false positives, and this needs to be taken care of during sample preparation.

To overcome the sensitivity and specificity challenges of a single sensor, we carefully look at all the spectograms together and provide an intuitive insight into the array processing. A MP flowing with the flow velocity of v_{flow} will excite two neighboring sensors after a time difference of $\Delta t \approx \Delta d/v_{flow}$, where Δd is the distance between the two sensors as shown in the zoomed version in Fig. 3. Therefore, a genuine response of a passing MP in a single sensor will sequentially excite the neighboring sensors with a time difference of Δt. On the other hand, a false positive response in a sensor will not generate the sequential responses in the neighboring sensors, and therefore, can be disregarded, as shown in the figure. In a similar fashion, a false negative can also be disregarded, if that is the only missing sensor response admits other sequential responses, as elaborated in Fig. 3. Therefore, intuitively, through cross-correlation of the sensor spectrogram, only genuine responses can be extracted out, while false positives and false negatives can be filtered.

To quantify this process, we represent the spectrogram outputs of the i^{th} sensor as $s_{freq,i}(t)$, where $i = 1, .., N$. The multi-dimensional cross-correlation of the spectrogram outputs can be represented as $\mathcal{R}(s_{freq,1}(t_1), s_{freq,2}(t_2), ..s_{freq,N}(t_N))$. In the ideal

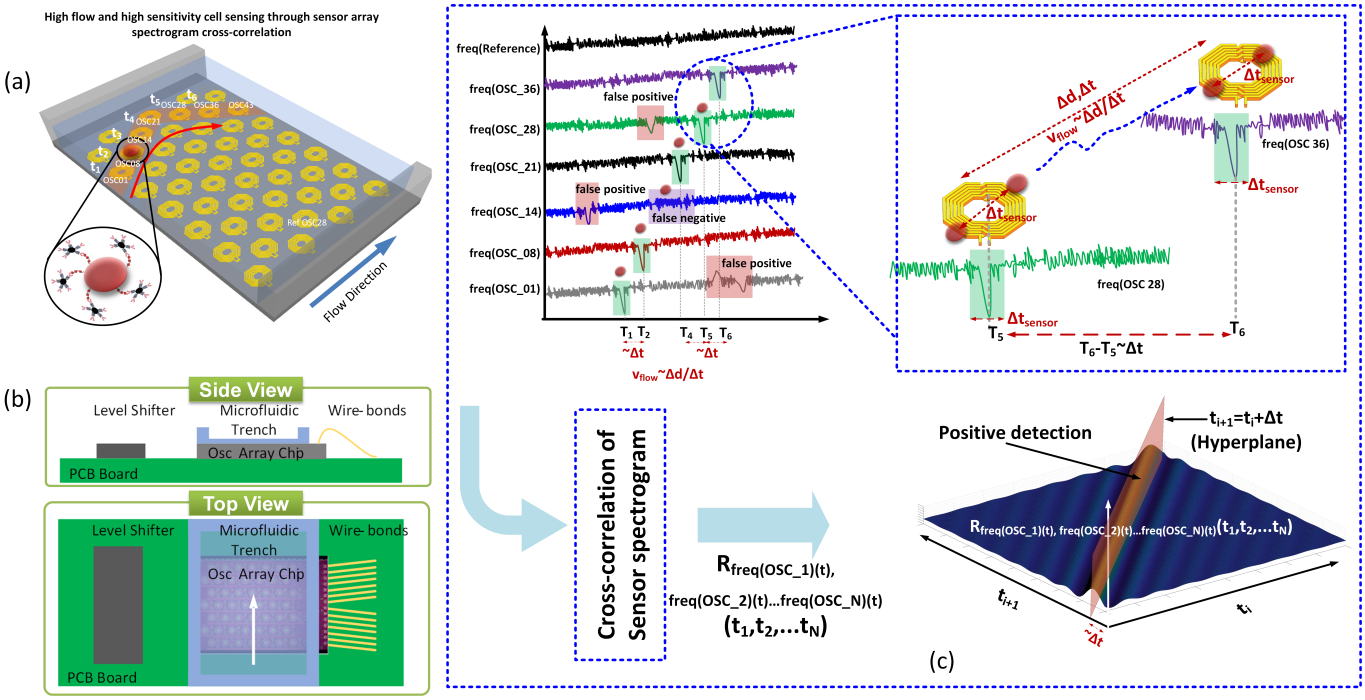

Fig. 3. High-throughput magnetic flow cytometer in CMOS with 2D array sensor processing (without focusing to a single sensor) and reduction of false positives/negatives with inter-site cross-correlation approach. (a) Illustration of a flow cell exciting sequentially an array of sensors in the 2D array chip. (b) Microfluidic packaging of the CMOS cytometer as the sample flows through a trench on the CMOS chip with a thin PDMS substrate separating the sample from the chip. (c) The spectrogram outputs of the sensors demonstrating expected downward frequency shifts as the magnetically tagged cell passes over the corresponding sensor (T_1, T_2, T_4, T_5, T_6), The example also shows illustrations of false positives, false negatives, high frequency oscillator noise and long term drifts. (d) As the spectrogram outputs are processed through a cross-correlator, the ideal output will demonstrate a peak at the hyperplane $t_N = t_{N-1} + \Delta t = t_{N-2} + 2\Delta t = .. = t_1 + (N-1)\Delta t$, where Δt is the delay between the sensor outputs as the cell moves from one sensor to the next. The multi-dimensional output when projected on the 2D plane of (t_i, t_{i+1}), it will peak at $t_{i+1} = t_i + \Delta t$.

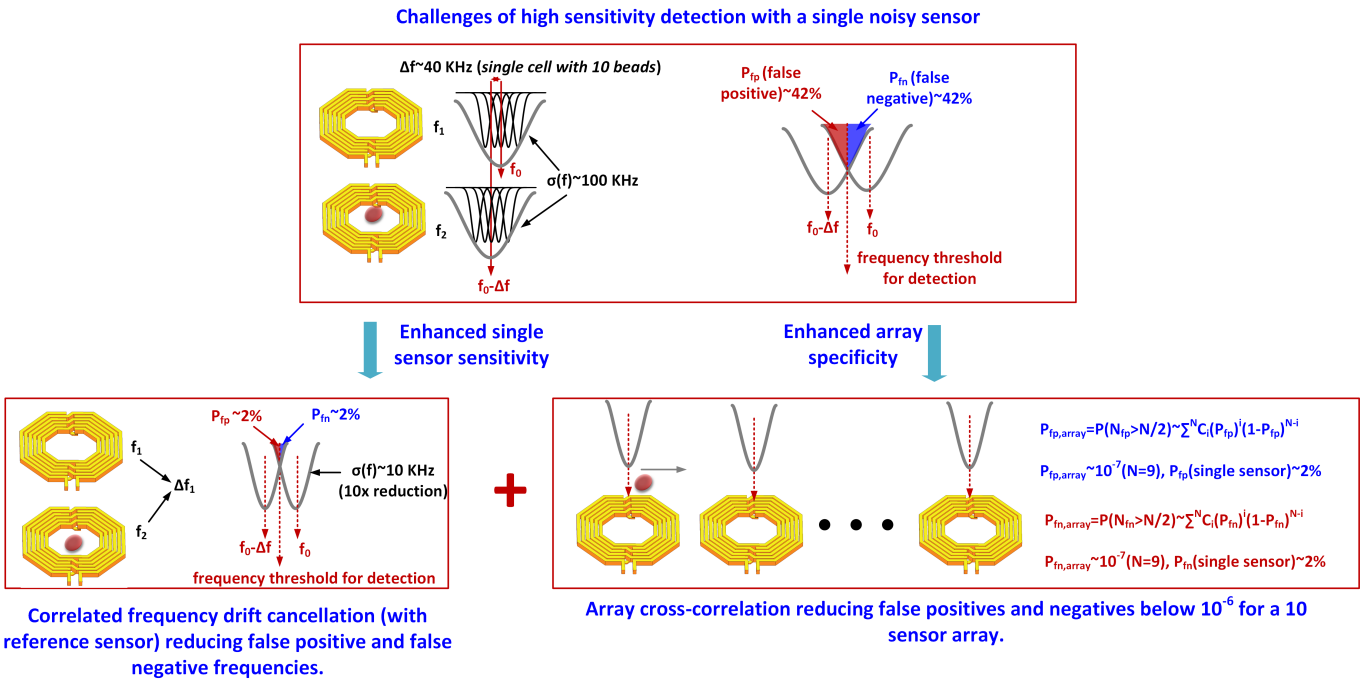

Fig. 4. Reduction of false and missing detection with 1) reduction of frequency variation through suppression of correlated drifts with a reference sensor (or inter-site suppression through dual frequency excitation) and 2) spectrogram cross-correlation and majority voting.

case, where a flowing MP excites a series of frequency pulses in the sensors sequentially with a time delay of Δt, $\mathbb{R}(s_{freq,1}(t_1), s_{freq,2}(t_2), ..s_{freq,N}(t_N))$ will spike in the hyperplane $t_N = t_{N-1} + \Delta t = t_{N-2} + 2\Delta t = .. =$

$t_1 + (N-1)\Delta t$. As illustrative purpose, when projected across the two dimension (t_i, t_{i+1}), the cross-correlation will peak at the hyperplane $t_{i+1} = t_i + \Delta t$, as shown in Fig. 3. Expectedly, the other spectrogram responses representing false positives and negatives will appear as small perturbations in the cross-correlation graph outside the plane, and therefore, needs to be neglected.

Evidently, the performance in array specificity through inter-site cross-correlation and rejection of false detections will improve with larger arrays. The principle is that larger arrays allow us to spatially sample the flowing array of MPs, observing more independent spectral outputs, thereby enabling further suppression of false responses. The sensor array also enables us to suppress low-frequency drifts of the sensors exploiting their correlation across the chip. This is illustrated in Fig. 4. As we will show in measurements later, the standard deviation of the frequency of the oscillators when measured over a 50-second timeframe shows a drift range of approximately 100 kHz. This fundamentally determines the sensitivity of a single sensor, as the frequency change due to a cell attached with ten 2.8µm beads is approximately Δf = 40 kHz. A decision boundary of a deviation of 20 kHz at the center, as illustrated in the figure, will result in false positives (P_{fp}) and negatives (P_{fn}) to be around an unacceptable range of 42%.

To overcome low-frequency drifts, we first use a reference oscillator to suppress correlated drifts [34]. Doing so, as we will demonstrate in measurements, squeezes the frequency drift standard deviation by an order of magnitude to approximately 10 kHz. This exponentially enhances the sensitivity by reducing the overlap area beyond the frequency threshold, and the false positive/negatives reduces to 2%. While this is an impressive reduction, this comes nowhere close to detecting rare cells or CTCs that requires specificity in the order of 1 parts per million. The inter-site cross correlation then utilizes the outputs of the drift-suppressed sensors to process them into a highly specific sensory output. The decision boundary in the spectrogram cross-correlation output sets the limits of achievability of false positives and false negatives. Consider false positive of a single sensor being $P_{fp} \approx 2\%$. Setting the cross-correlation threshold that is crossed only when all the N-sensors demonstrate a positive response reduces the false positive in the array sensing to ($P_{fp,array} = P_{fp}^N$). For N=8, the chances of false positives reduces near zero ($P_{fp,array} \approx 2\times10^{-14}$). However, this comes at a cost of false negatives, since we discard all responses until all the sensors have responded to the MP. The false negative stays at a single sensor level of $P_{fn} = 2\%$. Through a majority voting, both false positives and negatives can be reduced to the acceptable levels $P_{fp,array} \approx \sum_{i=N/2+1}^{N} {}^{N}C_i (P_{fp})^i (1-P_{fp})^{N-i}$ and $P_{fn,array} \approx \sum_{i=N/2+1}^{N} {}^{N}C_i (P_{fn})^i (1-P_{fn})^{N-i}$. For N=8, $P_{fp} \approx 2\%$, $P_{fn} \approx 2\%$, $P_{fp,array} = P_{fn,array} \approx 1.6\times10_{-7}$. This is illustrated in Table I.

TABLE I
TABLE SHOWS THE CORRESPONDING FALSE NEGATIVE RATE AND FALSE POSITIVE RATE V.S. THE NUMBER OF RESPONSE OF 9 SENSORS THAT NEED TO BE POSITIVE FOR POSITIVE OUTCOME

Number of Response	False Negative Rate of 9 Sensors	False Positive Rate of 9 Sensors
=9	1.66×10^{-1}	5.12×10^{-16}
≥8	1.31×10^{-2}	2.26×10^{-13}
≥7	6.13×10^{-4}	4.45×10^{-11}
≥6	1.86×10^{-5}	5.10×10^{-9}
≥5	3.78×10^{-7}	3.78×10^{-7}
≥4	5.10×10^{-9}	1.86×10^{-5}
≥3	4.45×10^{-11}	6.13×10^{-4}
≥2	2.26×10^{-13}	1.31×10^{-2}
≥1	5.12×10^{-16}	1.66×10^{-1}

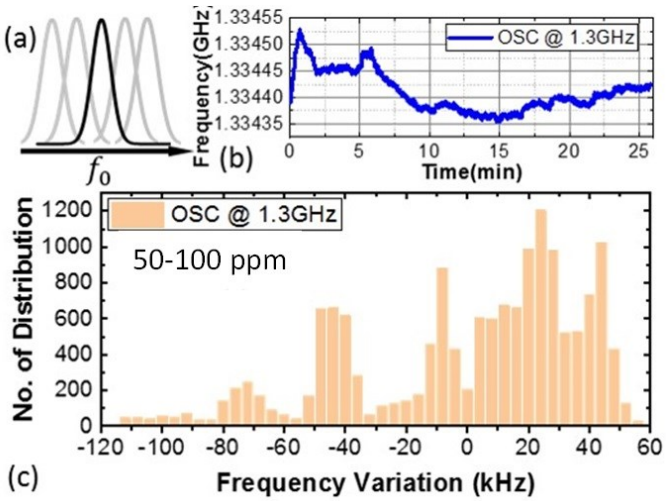

Fig. 5. Measured sensor oscillator frequency with time. (a) Representation of spectral drift. (b) Measured oscillator frequency output measured over 26 minutes of one of the sensor oscillators set at a frequency of 1.3 GHz. (c) Histogram of the frequency output showing a frequency variation range of 60-120 kHz (≈ 50-100 ppm) when measured over a 50 second time period.

III. Sensor Architecture, Circuits and Design Considerations

In this section, we will discuss multiple drift cancellation mechanisms to reduce the standard deviation of the frequency uncertainly, as illustrated earlier in Fig. 4. We will also discuss design of the single oscillator for enhance sensitivity and the 2D sensor architecture.

A. Drift Cancellation Mechanisms

We employ two separate methods for drift cancellation in the sensor array, one that uses a reference sensor and one that does not.

1) Drift cancellation with a reference sensor: As discussed previously, we utilize correlated drifts with a reference oscillator (shielded from the MPs) to cancel long term drifts [38]. It is expected that low frequency variations, such as that due to temperature changes, will have correlated drifts. Assuming a flow velocity of 1mm/s and a sensor size of 200 µm, a MP will pass through the sensor in 0.2 seconds. Therefore, close in phase noise and a low frequency drift above 50 Hz is important to consider. We will discuss the sensor design and the chip later, but Fig. 5 shows the measured frequency of oscillation of the implemented on-chip oscillator sensor (at 1.3 GHz) over a time period of 50 seconds. While the measured

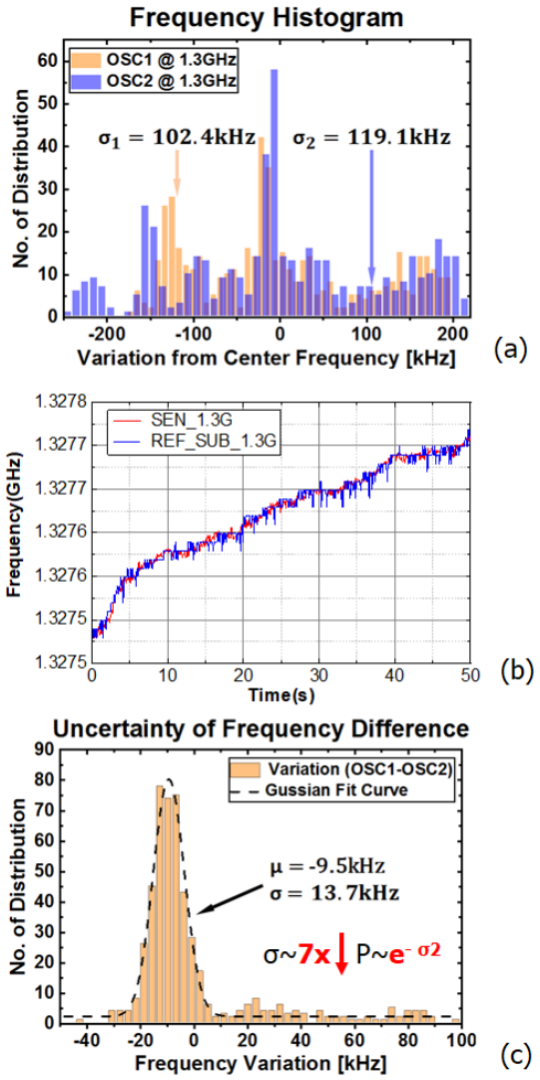

Fig. 6. Drift cancellation and squeezing of the frequency uncertainty in measurement with a reference sensor on-chip. (a) Frequency histogram of a sensor and a reference oscillator measured over 50 seconds showing standard deviations of the frequency variation of 102.4 kHz and 119.1 kHz respectively. (b) Measured spectral peaks of the sensor and reference oscillator showing highly correlated low-frequency drifts. (c) Reduction in the frequency uncertainty after suppression of correlated drifts. The standard deviation $\sigma(f)$ reduces by almost 7×, and the probability of false positives reduces exponentially.

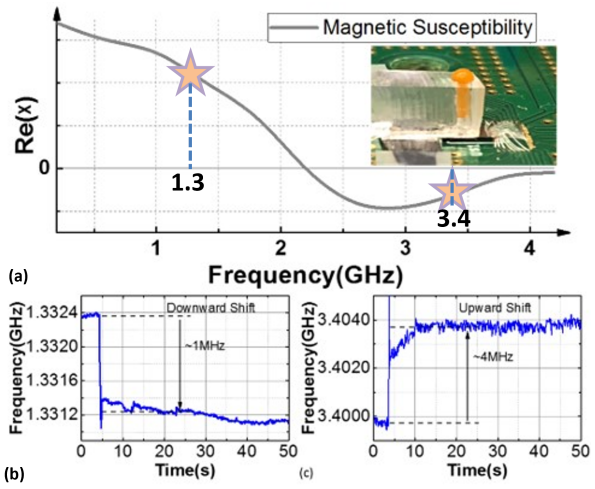

Fig. 7. Drift cancellation utilizing frequency dependence of the magnetic susceptibility of the superparamagnetic beads. (a) Magnetic susceptibility of the super-paramagnetic beads demonstrating $\chi \geq 0$ below 2.2 GHz and $\chi \leq 0$ between 2.2 and 4 GHz. (b) Measured sensor response to the beads showing a downward shift for sensors oscillating at 1.3 GHz and an increase in frequency for sensors operating at 3.4 GHz.

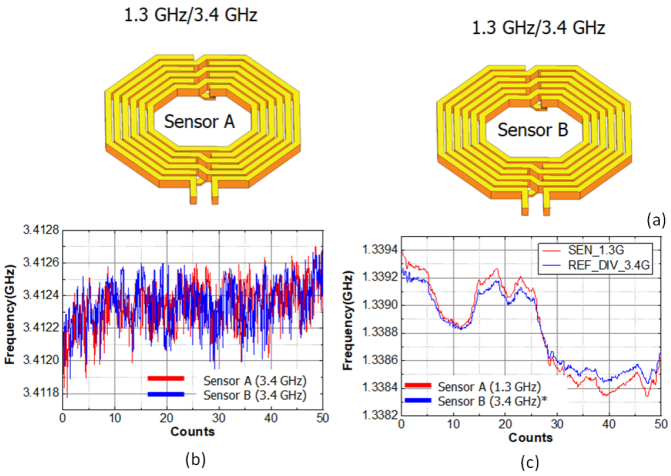

Fig. 8. Dual-frequency oscillatory sensors. (a) Two sensor sites with two independent oscillation frequencies at each sire. (b) Measured correlation of the drifts for reference and sensor oscillating at 3.4 GHz (c) High correlation of low-frequency drift is also observed when sensor is set at 1.3 GHz and reference is set at 3.4 GHz. Here, the reference sensor at 3.4 GHz is normalized to reflect the correlated drifts across the two frequencies.

timeframe is much longer than the passage of a MP over a sensor, the measurement gives us an estimate of the standard deviation of the frequency when measured for substantially long time periods. As shown in the measurement, the $\sigma(f)$ of a single sensor can vary between 60-110 kHz (50-100 ppm) depending on the length of the measurement time.

Fig. 6 shows the measurement results with a sensor oscillator and a reference oscillator demonstrating their variations, and correlation. As can be seen in Fig. 6(a), $\sigma(f)$ of both reference and sensor oscillator are reasonably close to being 102.4 and 119.1 kHz. Fig. 6(b) demonstrates their measured frequency of oscillation up to 50 seconds, when the frequency of oscillations are normalized to the same value at t=0. As expected, the drifts are highly correlated. When their correlated drifts are suppressed, the measured variation of their frequency difference narrows by a approximately 7× to $\sigma(f) \approx 13.7\text{kHz}$. This leads to an exponential reduction in the false positives and negatives, as elaborated in Section II, as $P_{fp,fn} \propto e^{-\sigma^2}$. The non-zero mean implies that one oscillator drifts with a higher bias than the other, potentially due to a temperature gradient on the chip. However, this does not affect the measurement uncertainty range.

2) Drift Cancellation with Dual-frequency Design: In addition to drift suppression with a separate reference sensor, we also implement inter-sensor drift compensation with a dual-frequency sensor design that utilizes the frequency dependence of the magnetic susceptibility of the biomarker [34]. The two

methods for drift cancellation allow us flexibility in designing system packaging and microfluidics and utilize one or the other, as the application demands. For example, with certain packaging it may not be possible to have the reference sensor shielded from the sample. In such cases, the inter-sensor drift cancellation will be useful.

Here, we use superparamagnetic beads as the biomarker called Dynabeads M-280 (Bangslabs PMC3HP) [31]. Superparamagnetic beads are made of polymer sphere that embeds nanometer-scale ferromagnetic particles, and their effective magnetic susceptibility is much larger than paramagnetic beads around zero DC magnetic field bias. In addition, the magnetic susceptibility of superparamagnetic beads has a frequency dependent response which is related to Neel relaxation time, as shown in Fig. 7(a) [39].

As can be seen from the figure, below 2GHz, the beads demonstrate a positive susceptibility ($\chi \geq 0$), as expected from a superparamagnetic bead. In this frequency range, a MP over a sensor leads to reduction in frequency of oscillation. However, as the oscillation time-period approaches the Neel relaxation time-period, the magnetic moments within the bead develops a lag with respect to the external oscillating field leading to a reduction of the susceptibility till it reaches value of zero at 2.2 GHz. When exited at this frequency, the beads essentially behaves as non-magnetic. Beyond 2.2 GHz, the susceptibility turns negative ($\chi \leq 0$). Utilizing this frequency-dependent effect, one can realize dual-frequency oscillators that switches between two frequencies in these two ranges (eg. 1.3 GHz and 3.4 GHz chosen in this design). In the presence of a MP, if the oscillator is switched rapidly between these two frequency of oscillations, the output spectrum will experience spectral shifts of $-\Delta f_1$ and Δf_2, while sharing the common drift. This allows a single sensor to suppress the long-term drift, through rapid switching between these two states.

The measured results of drift correlation at 3.4 GHz between a sensor and a reference oscillator is shown in Fig. 8. The dual frequency design not only allows us to suppress drift within a single sensor, it also allows the same with a reference sensor, with the latter operating at the higher frequency (3.4 GHz), while the sensor operates at the lower range (1.3 GHz). The drifts in the oscillation frequencies of the two sites are also highly correlated as shown in Fig. 8(b) and (c). This flexibility allows us to operate the reference at a different frequency than the sensor, thereby avoiding any spurious coupling to the sensor measurements and reducing sensitivity.

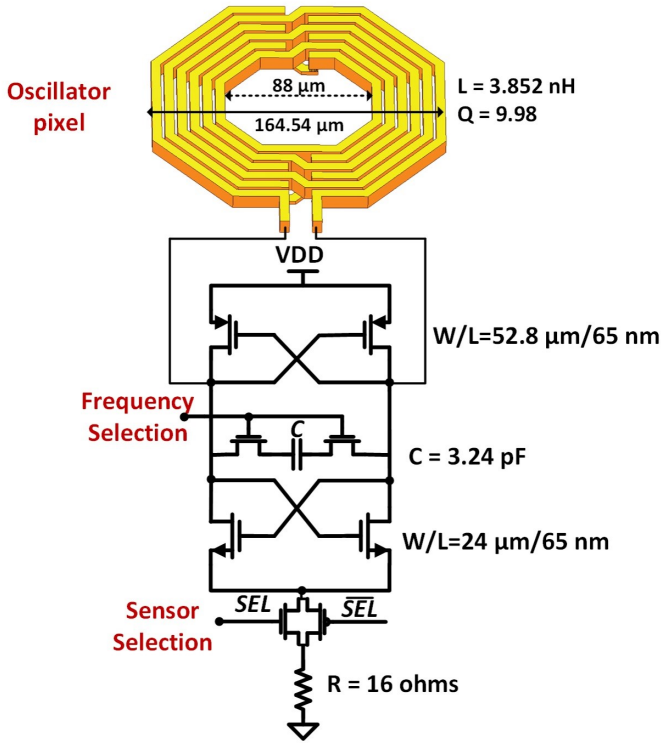

Fig. 9. Dual-frequency cross coupled oscillator circuit with a single inductor optimized for quality factor and enhance sensing area and a switchable capacitor bank.

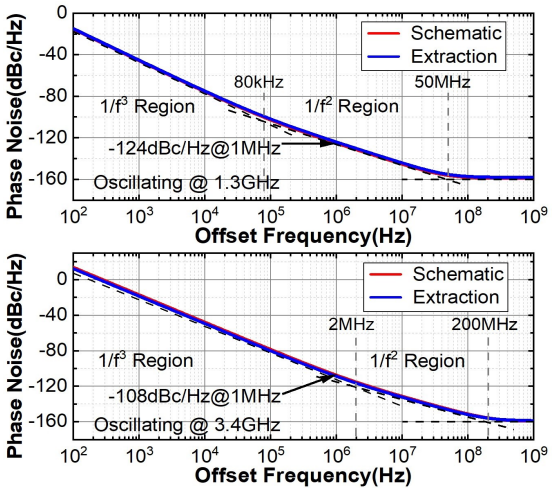

Fig. 10. Simulated phase noise for the dual-frequency oscillator at 1.3GHz and 3.4GHz.

B. Dual-frequency Oscillator Design

The circuit schematic of the dual-frequency oscillator is shown in Fig. 9. The frequency is chosen to be 1.3 GHz and 3.4 GHz to utilize the positive and negative susceptibilities of the MP (Fig. 7), while allowing a single inductor to serve in the oscillator tank. An inductor of value 3.85 nH is realized with a 164.5 µm diameter spiral geometry. The inductor diameter, trace widths and spacing were optimized simultaneously for quality factor (≈ 10) and increasing sensor area. A switchable capacitor bank of 3.2 pF capacitor is introduced into the oscillator to switch between the 1.3 and 3.4 GHz oscillation states. The simulated phase noise is for the two oscillation frequencies are -124dBc/Hz and -108dBc/Hz at 1 MHz offset. The reduction in phase noise at the higher frequencies is due to the switch losses of the capacitor bank.

In the presence of MP, the oscillator experiences a frequency shift of Δf, and the SNR can be defined as

$$SNR = \frac{\frac{\Delta f}{f_0}}{\sigma_{\frac{\Delta f}{f_0}}} \boxed{?} \frac{\frac{\Delta L}{L_0}}{\sigma_{\frac{\Delta f}{f_0}}} \quad (1)$$

where Δf is the sensor response due to an effective change

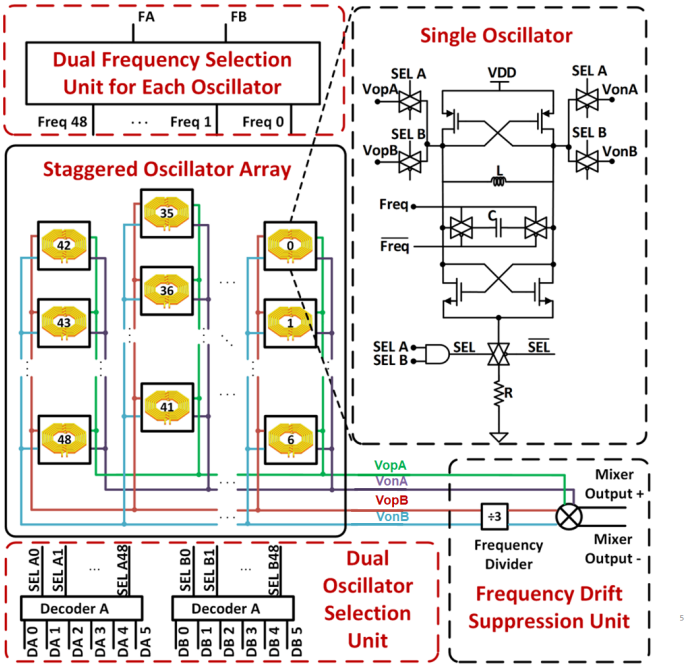

Fig. 11. The 2D sensor array architecture showing the honeycomb staggered sensor positions to capture all flowing MPs, dual-frequency selection unit, dual-oscillator selection unit and frequency drift suppression unit.

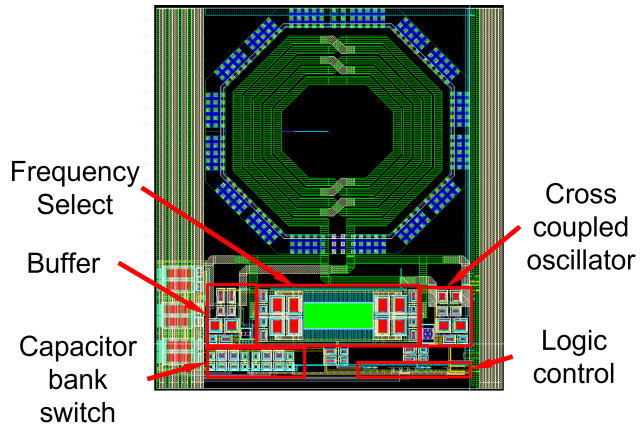

Fig. 12. The layout of a single sensor including the cross-coupled oscillator, buffer, the logic control unit, the frequency selection unit and the capacitor bank switch for frequency control.

of inductance (ΔL), and $\sigma_{\frac{\Delta f}{f_0}}$ represents the standard deviation due to noise and drift. The sensor noise floor $\sigma_{\frac{\Delta f}{f_0}}$ can be evaluated from the phase noise and is a function of the measurement time T_c. While longer measurement times can overcome the white noise portion of the phase noise, the contributions of $1/f^2$ and the $1/f^3$ due to integration during the measurement window T_c can be evaluated as [38]

$$\sigma^2_{\frac{\Delta f}{f_0}} = \frac{(\Delta f)^2}{(f_0)^2} = \frac{(\Delta T)^2}{(T_c)^2} = \sigma^2_{\frac{\Delta T}{T_c}} \quad (2)$$

$$\sigma^2_{\frac{\Delta f}{f_0}} = \frac{2}{\pi^2 f_0^2 T_c^2} \int_0^{+\infty} S_\varphi(f) \cdot \sin^2(\pi f T_c) df \quad (3)$$

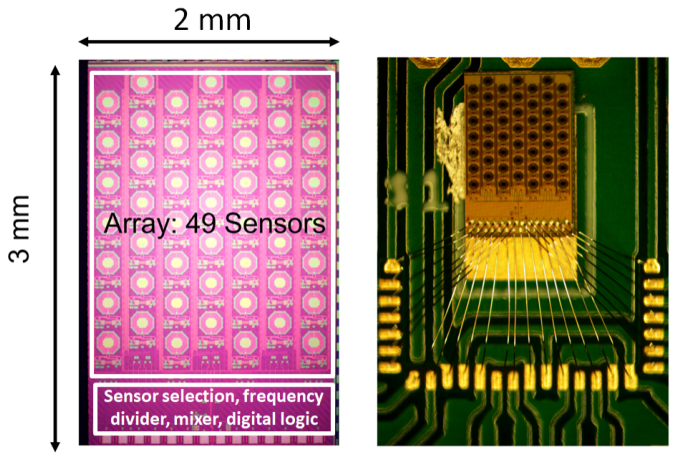

Fig. 13. Chip micrograph and wirebonding to interface with the microfluidics.

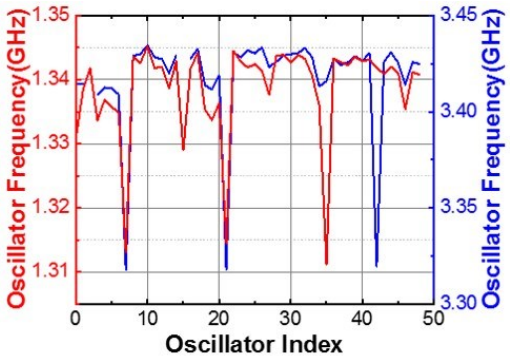

Fig. 14. Measured oscillation frequency of the 49 sensors set at 1.3 GHz and 3.4 GHz showing a sensor-to-sensor variation of 30 MHz and 100 MHz respectively at the two states.

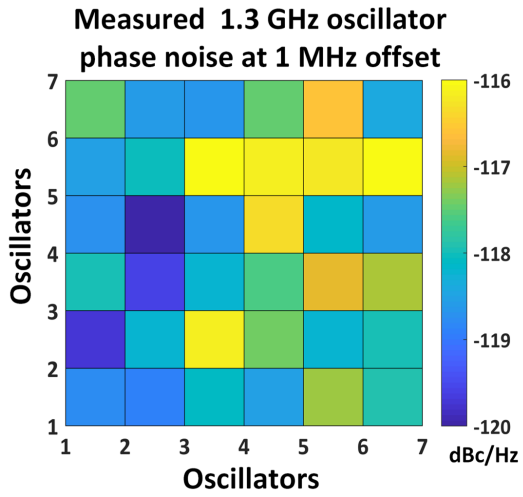

Fig. 15. Measured phase noise measured at 1 MHz offset for the 49 sensors set at 1.3 GHz.

This formulation allow us to estimate the effective SNR due to a change of inductance ΔL in presence of magnetic particles.

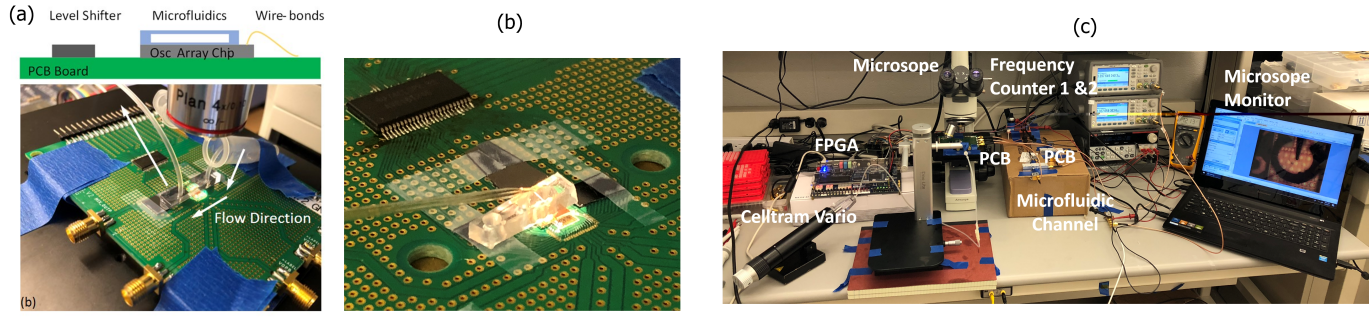

Fig. 16. Microfludic interface in our setup: (a) Side view of the integration of the CMOS and microfluidic channel; (b) Close-up view of the CMOS+fluidics set up. (c) Entire experimental set-up aided by real-time microscope imaging for ground truth showing velocities betwee 0.1-1 mm/s.

C. CMOS Microfluidic Integration and Sample Measurements

Fig. 2 shows picture of the testing platform and the packaging of the chip with the microfluidic channel. To ensure that the magnetic particles stay close to the sensor surface, the bottom PDMS substrate of the microfluidic channel is fabricated to be 30 µm thin. The microscope takes real-time images to allow for ground truth validation for cytometer measurements.

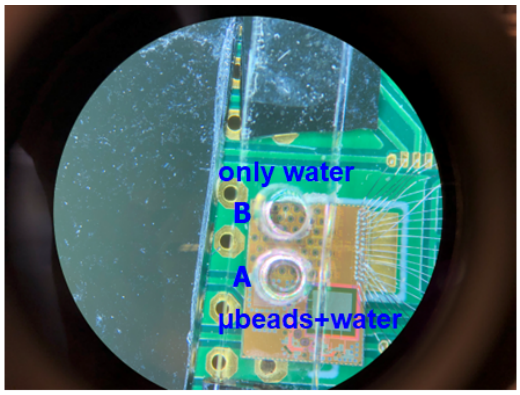

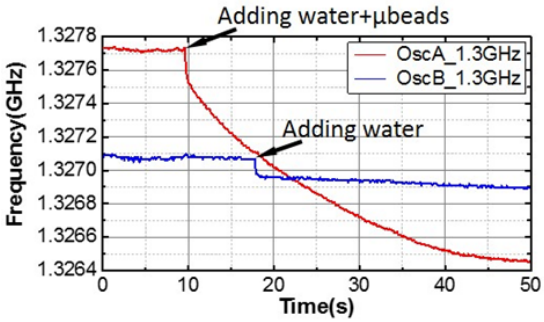

Fig. 17. Measured response of the sensor and reference oscillator when measured with plain water and water+super-paramagnetic beads demonstrating a clear downward frequency shift of the sensor frequency due to the presence of the magnetic beads.

$\sigma^2_{\frac{\Delta f}{f_0}}$ is the frequency measurement uncertainty, $S_\varphi(f)$ is the phase noise profile, T_c is total measurement time determined by the amount of time the cell tagged with MPs remain in the sensor area ($\Delta t_{sensor} \approx 0.2$s for v_{flow} ?1 mm/s) (Fig. 3). Based on the simulation of the phase noise in Fig. 10, $\sigma(f) \approx 10$ kHz. However, this does not take into consideration

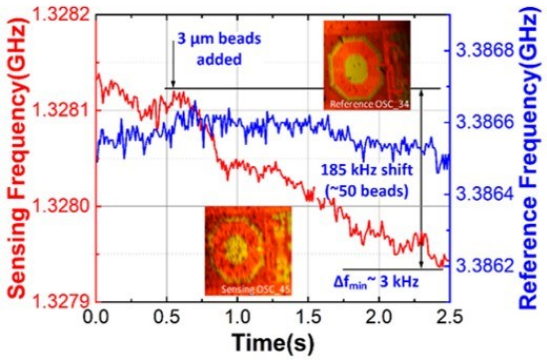

Fig. 18. Measurement of sensor sensitivity with respect to magnetic beads demonstrating approximately Δf of 3.7 kHz in the presence of one bead when the sensor is set at 1.3 GHz state.

low-frequency drifts due to temperature shifts, accounting for which increases $\sigma(f)$ to approximately 100-120 kHz that can be reduced further down to 10-15 kHz after suppression of correlated drift with a reference sensor, as shown in Fig. 4 and Fig. 6.

On the other hand, for a single 2.8 µm superparamagnetic Dynabeads ($\chi_{ext} \approx 0.11$ at 1.3GHz), a sensing inductor L ≈ 3.85 nH, and h ≈ 30µm between the sensor and the MP, the simulated frequency shift Δf is approximately 4kHz in vacuum ($\Delta f \approx 3$kHz in PBS). Therefore, while a single bead cannot be detected, a cell tagged with 10 beads results in a f=40 kHz (Fig. 4), that can be detected with a SNR ≈ 4. While all the beads tagged on the cell will not be near the bottom of the channel, this provides as a first order calculation of the expected frequency change. The sensitivity of the sensor decreases with distance as the near field falls as $1/r^3$ and $1/r^4$ from the surface [40].

D. Architecture of the Sensing Array Chip

The chip has four logical sections, shown in Fig. 11. Array section has 49 cross-coupled oscillators. Frequency control section can set the oscillating frequency of each individual sensor at either 1.3GHz or 3.4GHz. The decoder section helps us select one or two pixels work at each probing period. Mixer section allow us canceling the background frequency drift by using two pixels. With this architecture, we can select any one

or two pixels and set their oscillating frequency individually at 1.3 or 3.4 GHz.

The 2D sensor array has the 49 oscillators laid out in a honeycomb fashion to avoid missing any passing MP (Fig. 11). The oscillator outputs are buffered to allow to two simultaneous sensor readout at independently selected frequency states (1.3 or 3.4 GHz). The architecture includes another path where the output of the oscillators (sensor and reference) are directly mixed together to suppress correlated noise and then read out. If the reference and the sensor are set in a state of two different frequencies, then the higher frequency output (3.4 GHz) is frequency divided by 3 and then mixed with the other output. The architecture and layout of a single core is shown in Fig. 11 and Fig. 12 respectively. The sensors are enough such that spurious coupling through substrate or through air does not impact an frequency pulling.

IV. Measurement Results

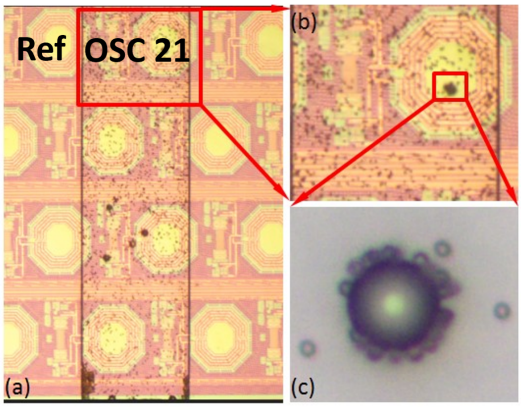

Fig. 19. Flowing test and magnetic cell model with a 16 µm polymer sphere-shaped particles (Spherotech TPX-150-5 Biotin Coated Polystyrene), each tagged with 10-20 with magnetic beads. (a) Microscopic image of the single pixel flowing test. (b) Zoomed image of the sensing pixel. (c) Zoomed image of the cell model.

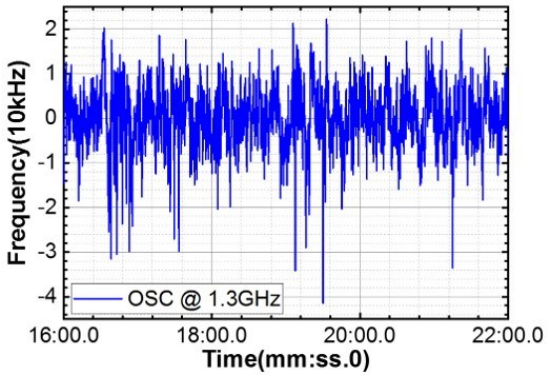

Fig. 20. Dynamic response of the single pixel (after drift suppression) in the flow test.

The chip was fabricated in a 65-nm CMOS process. The chip measures 2 mm × 3 mm as shown in Fig. 13. As can be seen, the wire-bonding is done on one side to place the microfluidic channel on top of the CMOS chip.

A. Sensor Characterization

Fig. 14 shows the measured oscillation frequencies of all the sensors when set at 1.3 and 3.4 GHz. As can be seen, the total frequency differences across the sensor operation frequency (due to process variations and mismatches) at the two frequency states of 1.3 and 3.4 GHz are around 30 MHz and 100 MHz respectively. The measured phase noise of the sensors at their 1.3 GHz oscillation state is shown in Fig. 15. The average phase noise at 1 MHz offset is around -120 dBc/Hz with approximately 4 dB difference across the sensors (Fig. 15). The difference can arise due to process variations, mismatches and the DC voltage distribution difference across the chip.

We perform preliminary measurements with sensor verification with magnetic beads as shown in Fig. 17. In this test, we focus on two sensors (OscA and OscB in Fig. 17) in the same chip operating in two separate chambers. We add water plus high concentration 3µm super parametric magnetic beads (ProMag 3 HP) to the OscA and only water to the OscB. As can be seen from the figure, there is a clear frequency difference between the two sensors due to the addition of the samples that is induced by the magnetic beads.

To quantify the sensitivity, we characterize the sensor response to 3 µm super parametric magnetic beads with respect to a reference sensor. Upon addition of the solution, the measured sensor and reference response show the gradual frequency drift as all the beads settle on the surface over a period of 2 seconds. The measured frequency shift of 185 kHz for around 50 such beads leads to a frequency change of the expected shift of 3.7 kHz for one bead as shown in Fig. 18, very close to the simulated value.

B. Flowing Test - Dynamic Measurements

We perform experiments with flow samples with cells tagged with magnetic particles. First, to quantify the frequency shift, we perform experiments with 16 µm polymer sphere-shaped particles (Spherotech TPX-150-5 Biotin Coated Polystyrene), each tagged with 10-20 with magnetic beads. This allows us to emulate flow of lymphoma cancer cells (with usual diameter in the range of 15-20 µm). Here, we use 2.8 µm superparamagnetic beads (M-280 streptavidin coated Dynabeads) as the magnetic label. First, we conduct a flowing test on a single pixel. In this experiment, oscillator 23 operates as the sensing pixel and the oscillator 21 operates as the reference pixel, shown in Fig. 19(a) and (b). The zoom picture of the sphere tagged with multiple magnetic cells is shown in Fig. 19(c). As the sample flows over the sensor, the dynamic spectrogram signal output (after drift cancellation) for a 6 minute period is shown in Fig. 20.

Fig. 21 shows the dynamic responses of single, double, triple and quadra cell models. The inset picture shows the passing of the cell model near the center of the sensor. As can be seen, each sensor response lasts for an estimated time of $\Delta t_{sensor} \approx 0.2$s, as estimated in previous discussion. The exact nature of the curve (including magnitude and time span) depends on the nature fo the cluster of the MPs, and their position relative to the sensing area. The magnitude of the

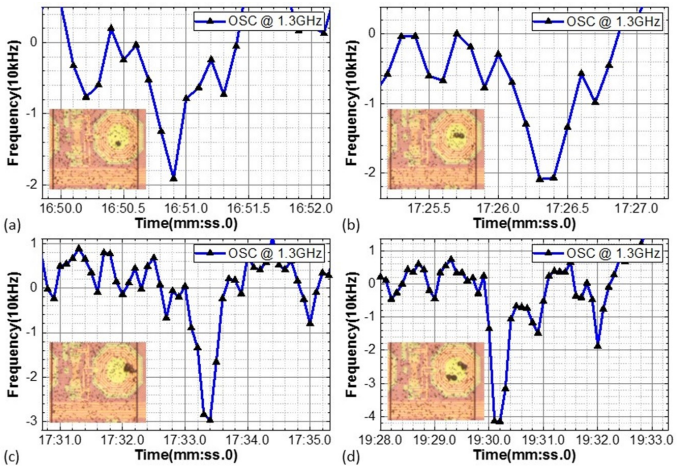

Fig. 21. Measured singe pixel response in the flow test to difference cell models representing varying sizes of the magnetic bead clusters. (a) Measured response of the single cell model, (b) double cell models, (c) triple cell model, and (d) quadra cell models.

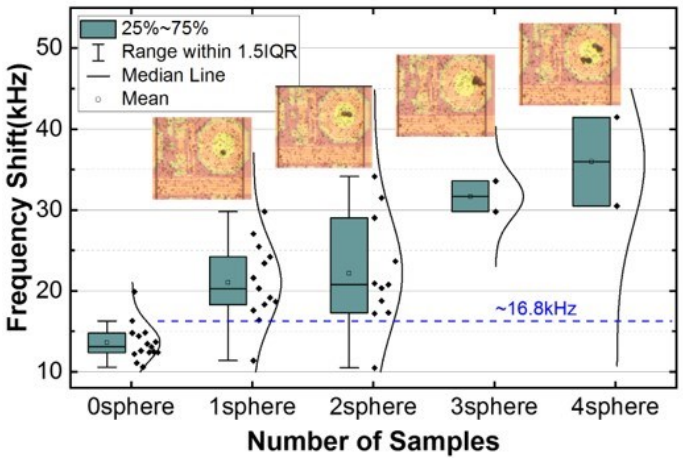

Fig. 22. Measured distributions of the sensing pixel frequency shift response corresponding to varying sizes of the magnetic bead clusters representing different sized cell models.

frequency shift increases with larger clusters and represented in the distribution in Fig. 22. While there is somewhat of a larger variation (due to low sample points), there is a clear shift in the average frequency shift as the cluster sizes increase from single to multi-cell models.

We measure the sensor response with cultured lymphoma cancer cells that are tagged with the 2.8 μm superparamagnetic Dynabeads (M-280) with an antimatriptase monoclonal antibody (M69) and an IgG-magnetic bead assembly (Fig. 23). While the single sensor response shows the ability to detect cells, the cross-correlation across multiple sensor sites is key to enabling cell tracking and reducing false positives/negatives. The measured sensor response when a cancer cell is placed with a celltram vario (Eppendorf) is shown in Fig. 23(b). We show real-time cell tracking ability across multiple sensors by allowing the cells to pass over the chip sensor area through microfluidic channels controlled with the celltram vario. An example is illustrated in Fig. 23(c), as the cell cluster passes through Sensor1 to Sensor2 and back to Sensor 1 sequentially, without going to Sensor 3. As expected, we see a downward frequency shift corresponding to the passage of the cell cluster over the particular sensor at the time periods $t_1, t_2, t-3, t_4$ without affecting the response from Sensor 3. The two peaks that we see in the blue curve could have happened as we added the sample to the chip, and this might have caused some disturbance in the chip and the interconnects.

We demonstrate the effect of suppression of false positives and negatives through the example illustrated in Fig. 24. Here, the cell cluster passes through multiple neighboring sensors (OSC02, OSC16, OSC30 and OSC44). Fig. 24(a) shows four time delayed signals on four pixels when one cell passes over them. We see the expected reduction in frequency at the exact time when the cell passes over the array. From these delayed signals, we can calculate the velocity of the cell model passing over the sensors (0.486 mm/s). This is a perfect detection case, where there are no false or missing detections. Fig. 24(b) and (c) show the results of the experiment repeated multiple times demonstrating false negatives. We see two cases of false negatives in Fig. 24(b), the sensor (OSC16 misses detection), and in Fig. 24(c) (OSC 02 misses detection). However, through cross-correlation of the other sensor responses and setting the threshold appropriately as elaborated in Section II, one can exponentially reduce false positives or negatives. This example with four sensors demonstrated the key proof-of-concept of the multi-sensor array processing, which when expanded to the entire array (with more than 10 sensors) can allow allow highly sensitive and highly specific real-time 2D cell tracking, extraction of flow velocities, and multiple-site detections while maintaining very low false positives and negatives in a high throughput flow.

The comparisons with other state-of-the-art cyclometers are presented in Table II. As can be seen, this is the first CMOS-based magnetic flow cytometer with multi-sensor array, requiring no external magnets, and allowing sensor output correlation for high sensitivity and specificity.

V. Conclusion

In this paper, we demonstrate a high throughput magnetic flow cytometer realizes with a microfluidics-packaged CMOS chip with a 2D staggered oscillator based magnetic sensor array. To overcome the noise issues of singular sensors, we implement drift suppression through the dual-frequency design and a reference oscillator, one of which or both may be used depending on the application. More importantly, to enhance sensitivity to allow for rare cell detection, we perform cross-correlation of the sensor spectrogram outputs that peaks at a temporal hyerplane depending on the velocity flow. By setting the threshold for cross-correlation detection, the probability of false and missing detection can be reduced to ppM levels. We demonstrate the chip functionality including response magnetic beads, magnetically-tagged cells and multi-site tracking and false/missing detection suppression with cultured lymphoma cancer cells.

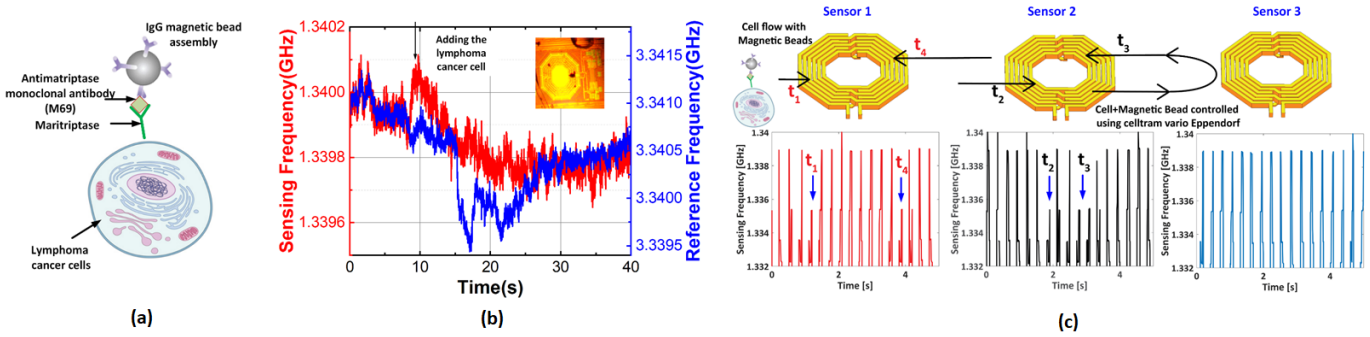

Fig. 23. Measured sensor with tagged lymphoma cancer cells. (a) Cultured lympohoma cancer cells that are tagged with the 2.8 μm super-paramagnetic Dynabeads (M-280) with an antimatriptase monoclonal antibody (M69) and an IgG-magnetic bead assembly. (b) Measured response when lymphoma cancer cell cluster with magnetic bead is added to the system. (c) Multi-site racking with sequential frequency perturbation as the cancer cell transits across the chip allowing real-time tracking and reduced false positive detections.

TABLE II
COMPARISON WITH PRIOR MINIATURIZED MAGNETIC FLOW CYTOMETERS (MFCs)

	[29]	[41]	[19]	[42]	[22]	This work
Sensing Principle	μHall Detector (PHEMT GaAs)	GMR Spin-valve	Spiral Transformer in 65nm CMOS	GMR Spin-valve	Multi-stripe GMR Spin-valve	LC Oscillator-based Frequency Shift in 65nm CMOS
Sensing Pixels	2×4	1×1	1×2	1×2	1×8	7×7
Operating Frequency	Baseband pulse	Baseband pulse	0.9/2.6GHz	Baseband pulse	Baseband pulse	1.3/3.4GHz
Readout Principle	Amplitude	Amplitude	Amplitude	Amplitude	Amplitude	Frequency Shift
Magnetic Field (mT)	500	100-170	10	100	60	None needed
Magnetic Labels	10-16 nm Self-synthesized Beads	200 nm nano-screenMAG/G-Biotin	0.8-1 μm Beads (OceanNanotech)	500 nm Bio-MasterBead Streptavidin	200 nm Bio-Adembeads Streptavitin	2.8 μm M-280 Streptavidin
Cell Model	MDA-MB-468 Cells	12 μm Polystyrene Beads	SKBR-3 Cells	SW480 Cells	10 μm Polystyrene Beads	Lymphoma cancer cells and 16 μm Polystyrene Beads
Flow Focusing Technique	Hydrodynamic Focusing & Chevron Pattern	Magnetophoretic & Mechanical	–	3D Hydrodynamic Focusing	Hydrodynamic focusing	No focusing needed for the 2D array
Sensing Medium	1×PBS	1×PBS	1×PBS	1×PBS	0.1×PBS	1×PBS
Signal Processing	Thresholding	Time of flight	Dual-frequency, thresholding & phase data	Time of flight	Matched Filtering, cross-correlation	Correlated noise suppression, dual frequencies, and inter-site cross-correlation (for false detection reduction)
SNR for Single Cell/Model	⍰5 dB	>5 dB	11 dB	17 dB	>14 dB	21.5 dB
Measurement time	0.02 ms	40 ms	10 ms	⍰ 1 ms	10nL/s	10 ms
Typical Accuracy	96%	N/A	>87%	N/A	95.26%	99.3%

ACKNOWLEDGMENTS

We acknowledge the support of National Science Foundation, Princeton Catalysis Initiative, Princeton Intellectual Property Fund, and Princeton Bartlett Fund. We also thank Philip Feng and Hao Jia (Case Western Reserve University, Dept. ECE) for lending us the Celltram Vario system and fabricating the single cell manipulation pipette. We also acknowledge Gulam M. Rather, Joseph R. Bertino, Chen-Yong Lin for providing us the cell lines.

Hao Tang received the B.S. in Electrical Engineering in 2016. He joined the IMRL Lab in 2018 and received the M.S.E. degree from Electrical and Computer Engineering at Princeton University in 2023. His research interests include developing new architectures for point-of–care diagnostics and chip-scale platforms for cellular assays. In particular, he has been interested in high throughput, pneumatic-free, cytometry with high specificity and sensitivity.

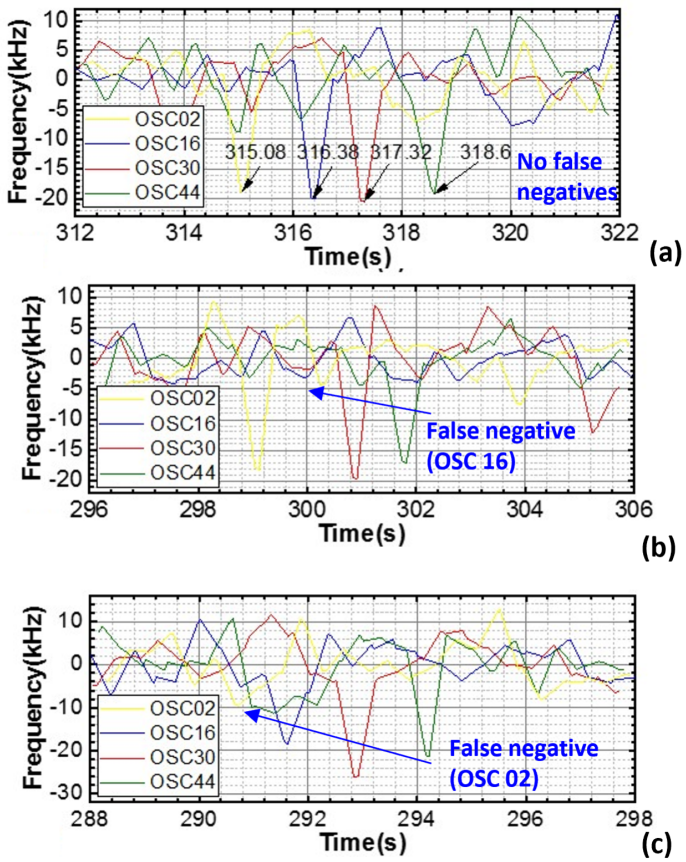

Fig. 24. Measured multi-site tracking for inter-site cross-correlation and reduction of false positives. (a) Measured response of the flowing tagged lymphoma cell across four sensors, all demonstrating detection with a time lag of 100 ms that is dependent on the flow velocity. (b) Same experiment repeated when the sensor (OSC16) misses the cell showing false negative. (c) Same experiment repeated when the sensor (OSC02) misses the cell showing false negative. The inter-site cross-correlation and its threshold setup can suppress any such false/missing detection for enabling high throughput and high specificity cytometers.

Suresh Venkatesh (Senior Member, IEEE) received his M.S. degree in Electrical and Computer Engineering from North Carolina State University in 2010 and his Ph.D. in Electrical and Computer Engineering from the University of Utah in 2017. His PhD dissertation received the ECE Outstanding Dissertation Award, in 2016. He is currently an Assistant Professor at North Carolina State University, Electrical and Computer Engineering Department.

Prior to joining NC State, he was an Associate Research Scholar at the Electrical and Computer Engineering Department, Princeton University, and a lead antenna technology consultant for Massachusetts-based start-ups namely, Wafer LLC and E-Space where he developed SATCOM technologies for high-speed low-latency communications. He was also a Research Project Assistant at Molecular Astronomy Laboratory, Raman Research Institute, Bangalore during 2007-08, where he worked on a millimeter-wave radio telescope. His research interests are in electromagnetics, metamaterials, antenna design, integrated circuits, computational imaging, and transformation optics design. He is a recipient of the 2021 Mistletoe Research Fellowship from the Momental Foundation. He is an affiliate member of the MTT-23 Wireless Communication and MTT-21 Terahertz Technology and Applications committees. He serves as the technical program committee co-chair for World Microwave Congress, 2024.

Zhongtian Lin Zhongtian Lin received the PhD in Electrical Engineering from Rutgers University New Brunswick in 2020. He is currently a senior research engineer at RizLab Heath, Inc. His research interests lie in biomedical electronics, microfluidics, and diagnostic test development.

Xuyang Lu (Member, IEEE) received the B.S. degree in electrical engineering from Rice University, Houston, TX, USA, in 2014, and the M.A. and Ph.D. degrees in electrical engineering from Prince838 ton University, Princeton, NJ, USA, in 2016 and 2020, respectively.

He joined as a Faculty Member with the University of Michigan-Shanghai Jiao Tong University Joint Institute, Shanghai Jiao Tong University, Shanghai, China, in 2021, with a joint appointment with the Department of Electronic Engineering. He is also a member of the MoE Key Laboratory of High-Speed Electronic Systems, Shanghai Jiao Tong University. His research interests include high-speed pro847 grammable RF and mmWave integrated systems, integrated terahertz systems, integrated photonics, on-chip antenna optimization, and machine-learning in analog circuit design.

Hooman Saeidi received the bachelor's degree in electrical engineering from the Sharif University of Technology, Tehran, Iran, in 2017.

He received the PhD degree from Electrical and Computer Engineering, Princeton University, Princeton, NJ, USA in 2023. His research interests include electromagnetics, mm-Wave, and THz circuits and integrated circuits for high data rate communication systems.

Mehdi Javanmard is a Professor in the Electrical and Computer Engineering Department at Rutgers University. He received the BS (2002) from Georgia Institute of Technology and the MS (2004) and PhD (2008) all in electrical engineering from Stanford University. During his time at Stanford, he worked on the development of electronic microfluidic platforms for low-cost genomic and proteomic biomarker detection, and later worked as a Senior Research Engineer at the Stanford Genome Technology Center. In Fall 2014, he joined the Electrical and Computer Engineering Department, Rutgers University as an Assistant Professor. His research interests include developing portable and wearable technologies for continuous health monitoring and understanding the effects of the environment on health.

In 2017, he was recipient of the Translational Medicine and Therapeutics Award by the American Society for Clinical Pharmacology and Therapeutics for his group's work in point of care diagnostic tools for assessing patient response to cancer therapies. He has received various awards as a Principal Investigator from the National Science Foundation, National Institutes of Health, DARPA, and the PhRMA foundation to support his research. He was awarded the National Science Foundation CAREER Award for young faculty in 2019 and the DARPA Young Faculty Award in 2020. In 2018, he co-founded RizLab Health, a startup company dedicated to enabling point-of-care hematology analysis.

Kaushik Sengupta (Senior Member, IEEE) received the B.Tech. and M.Tech. degrees in electronics and electrical communication engineering from IIT Kharagpur, Kharagpur, India, in 2007, and the M.S. and Ph.D. degrees in electrical engineering from the California Institute of Technology (Caltech), Pasadena, CA, USA, in 2008 and 2012, respectively. In 2013, he joined the Department of Electrical and Computer Engineering, Princeton University, Princeton, NJ, USA, as a Faculty Member, where he is currently Professor and Director of the Integrated Microsystems Research Lab. His current research interests include high-frequency integrated circuits (ICs), electromagnetics, and optics for various applications in sensing, imaging, and high-speed communication.

Dr. Sengupta received the DARPA Young Faculty Award in 2018, the Bell Labs Prize in 2017, the Young Investigator Program Award from the Office of Naval Research in 2017, the E. Lawrence Keys, Jr. Emerson Electric Co. Junior Faculty Award from the Princeton School of Engineering and Applied Science in 2018, and the Excellence in Teaching Award in 2018 nominated by the Undergraduate and Graduate Student Council in the Princeton School of Engineering and Applied Science. He was a recipient of the Charles Wilts Prize in 2013 from Electrical Engineering, Caltech, for the best Ph.D. thesis, the Caltech Institute Fellowship, the Prime Minister Gold Medal Award of IIT in 2007, and the inaugural Young Alumni Achievement Award from IIT Kharagpur. He was a co-recipient of the IEEE Radio Frequency Integrated Circuits (RFIC) Symposium Best Student Paper Award in 2012, multiple best student paper awards in IEEE IMS, and the 2015 Microwave Prize from the IEEE Microwave Theory and Techniques Society. He has served as the Chair for Emerging Technologies for IEEE Custom Integrated Circuits Conference (CICC) in 2022. He is on the Technical Program Committee of International Solid-State Circuits Conference (ISSCC) in the Technology Directions Sub-Committee. He served as a Distinguished Lecturer for the IEEE Solid-State Circuits Society from 2019 to 2020, and as Distinguished Lecturer for the IEEE Microwave Theory from 2021-2023. He received the Outstanding Young Engineer Award from IEEE Microwave Theory and Techniques in 2021, and the IEEE Solid-State Circuits New Frontier Award in 2022. He currently serves as a co-chair of Chair of the IEEE Solid-State Circuits Directions Committee, and as a technical advisor for the wireless startup Guru Inc., based in Pasadena.

REFERENCES

[1] S. F. Ibrahim and G. van den Engh, "Flow cytometry and cell sorting," Cell separation: fundamentals, analytical and preparative methods, pp. 19–39, 2007.

[2] K.-H. Lee, J. Nam, S. Choi, H. Lim, S. Shin, and G.-H. Cho, "A cmos impedance cytometer for 3d flowing single-cell real-time analysis with $\Delta\Sigma$ error correction," IEEE Xplore, p. 304–306, 02 2012. [Online]. Available: https://ieeexplore.ieee.org/abstract/document/6177024

[3] J.-C. Chien, M. Anwar, E.-C. Yeh, L. P. Lee, and A. M. Niknejad, "A 6.5/17.5-ghz dual-channel interferometer-based capacitive sensor in 65-nm cmos for high-speed flow cytometry," IEEE Xplore, p. 1–4, 06 2014. [Online]. Available: https://ieeexplore.ieee.org/document/6848507

[4] C. Zhu, J. Maldonado, and K. Sengupta, "Cmos-based electrokinetic microfluidics with multi-modal cellular and bio-molecular sensing for end-to-end point-of-care system," IEEE transactions on biomedical circuits and systems, vol. 15, no. 6, pp. 1250–1267, 2021.

[5] S. R. Kumashi, D. Jung, J. Park, S. T. Sanz, S. Grijalva, A. Wang, S. Li, H. C. Cho, C. M. Ajo-Franklin, and H. Wang, "A cmos multi-modal electrochemical and impedance cellular sensing array for massively paralleled exoelectrogen screening," IEEE Transactions on Biomedical Circuits and Systems, vol. 15, no. 2, pp. 221–234, 2021.

[6] D. Jung, G. V. Junek, J. S. Park, S. R. Kumashi, A. Wang, S. Li, S. I. Grijalva, N. Fernandez, H. C. Cho, and H. Wang, "A cmos 21 952-pixel multi-modal cell-based biosensor with four-point impedance sensing for holistic cellular characterization," IEEE Journal of Solid-State Circuits, vol. 56, no. 8, pp. 2438–2451, 2021.

[7] M. Godin, F. F. Delgado, S. Son, W. H. Grover, A. K. Bryan, A. Tzur, P. Jorgensen, K. Payer, A. D. Grossman, M. W. Kirschner, and S. R. Manalis, "Using buoyant mass to measure the growth of single cells," Nature Methods, vol. 7, p. 387–390, 05 2010. [Online]. Available: https://www.nature.com/articles/nmeth.1452

[8] X. Ding, S.-C. S. Lin, B. Kiraly, H. Yue, S. Li, I.-K. Chiang, J. Shi, S. J. Benkovic, and T. J. Huang, "On-chip manipulation of single microparticles, cells, and organisms using surface acoustic waves," Proceedings of the National Academy of Sciences, vol. 109, pp. 11 105–11 109, 06 2012.

[9] G.-Y. Kim, J.-I. Han, and J.-K. Park, "Inertial microfluidics-based cell sorting," BioChip Journal, vol. 12, pp. 257–267, 12 2018.

[10] S. J. Altschuler and L. F. Wu, "Cellular heterogeneity: Do differences make a difference?" Cell, vol. 141, no. 4, pp. 559–563, 2010.

[11] L. Hong, H. Li, H. Yang, and K. Sengupta, "Fully integrated fluorescence biosensors on-chip employing multi-functional nanoplasmonic optical structures in cmos," IEEE Journal of Solid-State Circuits, vol. 52, no. 9, pp. 2388–2406, 2017.

[12] ——, "Integrated angle-insensitive nanoplasmonic filters for ultraminiaturized fluorescence microarray in a 65 nm digital cmos process," ACS Photonics, vol. 5, no. 11, pp. 4312–4322, 2018.

[13] H. Wang, "Magnetic sensors for diagnostic medicine: Cmos-based magnetic particle detectors for medical diagnosis applications," IEEE Microwave Magazine, vol. 14, no. 5, pp. 110–130, 2013.

[14] L. Hong, S. McManus, H. Yang, and K. Sengupta, "A fully integrated cmos fluorescence biosensor with on-chip nanophotonic filter," in 2015 Symposium on VLSI Circuits (VLSI Circuits). IEEE, 2015, pp. C206–C207.

[15] L. Hong and K. Sengupta, "Fully integrated optical spectrometer in visible and near-ir in cmos," IEEE transactions on biomedical circuits and systems, vol. 11, no. 6, pp. 1176–1191, 2017.

[16] L. Hong, H. Li, H. Yang, and K. Sengupta, "Nano-plasmonics and electronics co-integration in cmos enabling a pill-sized multiplexed fluorescence microarray system," Biomedical optics express, vol. 9, no. 11, pp. 5735–5758, 2018.

[17] C. Zhu, L. Hong, H. Yang, and K. Sengupta, "A packaged multiplexed fluorescent biomolecular sensor array and ultralow-power wireless interface in cmos for ingestible electronic applications," IEEE Sensors Journal, vol. 22, no. 24, pp. 24 060–24 074, 2022.

[18] C. Zhu, Y. Wen, T. Liu, H. Yang, and K. Sengupta, "An ingestible pill with cmos fluorescence sensor array, bi-directional wireless interface and packaged optics for in-vivo bio-molecular sensing," IEEE Transactions on Biomedical Circuits and Systems, 2023.

[19] P. Murali, A. M. Niknejad, and B. E. Boser, "Cmos microflow cytometer for magnetic label detection and classification," IEEE Journal of Solid-State Circuits, vol. 52, no. 2, pp. 543–555, 2017.

[20] M. Helou, M. Reisbeck, S. F. Tedde, L. Richter, L. Bar, J. J. Bosch, R. H. Stauber, E. Quandt, and O. Hayden, "Time-of-flight magnetic flow cytometry in whole blood with integrated sample preparation," Lab on a Chip, vol. 13, p. 1035, 2013.

[21] R. Soares, V. C. Martins, R. Macedo, F. A. Cardoso, S. A. Martins, D. M. Caetano, P. H. Fonseca, V. Silvério, S. Cardoso, P. P. Freitas, and et al., "Go with the flow: advances and trends in magnetic flow cytometry," Analytical and Bioanalytical Chemistry, vol. 411, no. 9, p. 1839–1862, 2019.

[22] C. C. Huang, P. Ray, M. Chan, X. Zhou, and D. A. Hall, "An aptamer-based magnetic flow cytometer using matched filtering," Biosensors and Bioelectronics, vol. 169, p. 112362, 2020.

[23] D. A. Hall, R. S. Gaster, K. A. Makinwa, S. X. Wang, and B. Murmann, "A 256 pixel magnetoresistive biosensor microarray in 0.18 μm cmos," IEEE journal of solid-state circuits, vol. 48, no. 5, pp. 1290–1301, 2013.

[24] X. Zhou, M. Sveiven, and D. A. Hall, "A cmos magnetoresistive sensor front-end with mismatch-tolerance and sub-ppm sensitivity for magnetic immunoassays," IEEE Transactions on Biomedical Circuits and Systems, vol. 13, no. 6, pp. 1254–1263, 2019.

[25] X. Zhou, E. Mai, M. Sveiven, C. Pochet, H. Jiang, C.-C. Huang, and D. A. Hall, "A 9.7-nt, 704-ms magnetic biosensor front-end for detecting magneto-relaxation," IEEE Journal of Solid-State Circuits, vol. 56, no. 7, pp. 2171–2181, 2021.

[26] D. M. Caetano, R. Afonso, A. R. Soares, J. Silva, H. I. Busse, V. Silverio, T. Rabuske, G. N. Tavares, J. R. Fernandes, and S. Cardoso, "Artificial neural networks for gmr-based magnetic cytometry," IEEE Transactions on Instrumentation and Measurement, vol. 72, pp. 1–11, 2023.

[27] K. Fodil, M. Denoual, C. Dolabdjian, M. Harnois, and V. Senez, "Dynamic sensing of magnetic nanoparticles in microchannel using GMI technology," IEEE Transactions on Magnetics, vol. 49, no. 1, pp. 93–96, 2013.

[28] K. Fodil, M. Denoual, C. Dolabdjian, A. Treizebre, and V. Senez, "In-flow detection of ultra-small magnetic particles by an integrated giant magnetic impedance sensor," Applied Physics Letters, vol. 108, no. 17, p. 173701, 2016.

[29] D. Issadore, J. Chung, H. Shao, M. Liong, A. A. Ghazani, C. M. Castro, R. Weissleder, and H. Lee, "Ultrasensitive Clinical Enumeration of Rare Cells ex Vivo Using a Micro-Hall Detector," Science Translational Medicine, vol. 4, 2012.

[30] D. Issadore, H. J. Chung, J. Chung, G. Budin, R. Weissleder, and H. Lee, "μHall Chip for Sensitive Detection of Bacteria," Advanced healthcare materials, vol. 2, no. 9, pp. 1224–1228, 2013.

[31] G. Fonnum, C. Johansson, A. Molteberg, S. Mørup, and E. Aksnes, "Characterisation of Dynabeads® by magnetization measurements and Mossbauer spectroscopy," Journal of Magnetism and Magnetic Materials, vol. 293, no. 1, pp. 41–47, 2005.

[32] Hua Wang, Yan Chen, A. Hassibi, A. Scherer, and A. Hajimiri, "A frequency-shift cmos magnetic biosensor array with single-bead sensitivity and no external magnet," in 2009 IEEE International Solid-State Circuits Conference - Digest of Technical Papers, Feb 2009, pp. 438–439,439a.

[33] H. Wang, A. Mahdavi, D. A. Tirrell, and A. Hajimiri, "A magnetic cell-based sensor," Lab Chip, vol. 12, pp. 4465–4471, 2012. [Online]. Available: http://dx.doi.org/10.1039/C2LC40392G

[34] C. Sideris, P. P. Khial, and A. Hajimiri, "Design and implementation of reference-free drift-cancelling CMOS magnetic sensors for biosensing applications," IEEE J. Solid-State Circuits, vol. 53, no. 11, pp. 3065–3075, 2018.

[35] L. Zhang, A. Ameri, M. Anwar, and A. M. Niknejad, "A microwave-optical biosensor with 5.4 ppm label/reference-free long-term stability and single photon sensitivity in 28nm bulk cmos," in 2019 IEEE Custom Integrated Circuits Conference (CICC). IEEE, 2019, pp. 1–4.

[36] J.-C. Chien and A. M. Niknejad, "Oscillator-based reactance sensors with injection locking for high-throughput flow cytometry using microwave dielectric spectroscopy," IEEE Journal of Solid-State Circuits, vol. 51, no. 2, pp. 457–472, 2015.

[37] H. Tang, S. Venkatesh, Z. Lin, X. Lu, H. Saeidi, G. M. Rather, J. R. Bertino, C.-Y. Lin, M. Javanmard, and K. Sengupta, "2d magnetic sensor array for real-time cell tracking and multi-site detection with increased robustness and flow-rate," in 2019 IEEE Custom Integrated Circuits Conference (CICC). IEEE, 2019, pp. 1–4.

[38] H. Wang, C.-C. Weng, and A. Hajimiri, "Phase noise and fundamental sensitivity of oscillator-based reactance sensors," IEEE Transactions on Microwave Theory and Techniques, vol. 61, no. 5, pp. 2215–2229, 2013.

[39] C. Sideris and A. Hajimiri, "An integrated magnetic spectrometer for multiplexed biosensing," in 2013 IEEE International Solid-State Circuits Conference Digest of Technical Papers. IEEE, 2013, pp. 300–301.

[40] H. Wang, Precision frequency and phase synthesis techniques in integrated circuits for biosensing, communication and radar. California Institute of Technology, 2009.

[41] M. Reisbeck, M. J. Helou, L. Richter, B. Kappes, O. Friedrich, and O. Hayden, "Magnetic fingerprints of rolling cells for quantitative flow cytometry in whole blood," Scientific reports, vol. 6, no. 1, p. 32838, 2016.

[42] A. Chicharo, M. Martins, L. C. Barnsley, A. Taouallah, J. Fernandes, B. F. Silva, S. Cardoso, L. Dieguez, B. Espiña, and P. P. Freitas, "Enhanced magnetic microcytometer with 3d flow focusing for cell enumeration," Lab on a Chip, vol. 18, no. 17, pp. 2593–2603, 2018.